# Numerical Modeling Studies of Wake Vortex Transport and Evolution Within the Planetary Boundary Layer

NASA Grant NCC-1-188



FY 97 Annual Report

submitted to the
NASA Langley Research Center

**Yuh-Lang Lin**
**S. Pal Arya**
**Michael L. Kaplan**
**Shaohua Shen**

Department of Marine, Earth and Atmospheric Sciences
North Carolina State University
Raleigh, NC 27695-8208
(919) 515-1438

April, 1998

# Contents

# 1 Objectives and Goals of the Research

In support of the wake vortex effect of the Terminal Area Producitivity program, we have put forward four tasks to be accomplished in our proposal. The first task is validation of two-dimensional wake vortex-turbulence interaction. The second task is investigation of three-dimensional interaction between wake vortices and atmospheric boundary layer (ABL) turbulence. The third task is ABL studies. The fourth task is addition of a Klemp-Durran condition at the top boundary for TASS model. The accomplishment of these tasks will increase our understanding of the dynamics of wake vortex and improve forecasting systems responsible for air safety and efficiency.

The first two tasks include following three parts: a) Determine significant length scale for vortex decay and transport, especially the length scales associated with the onset of Crow instability (Crow, 1970). (b) Study the effects of atmospheric turbulence on the decay of the wake vortices. (c) Determine the relationships between decay rate, transport properties and atmospheric parameters based on large eddy simulation (LES) results and the observational data. These parameters may include turbulence kinetic energy, dissipation rate, wind shear and atmospheric stratification.

The ABL studies cover LES modeling of turbulence structure within planetary boundary layer under transition and stable stratification conditions. Evidences have shown that the turbulence in the stable boundary layer can be highly intermitten and the length scales of eddies are very small compared to those in convective case. We proposed to develop a nesting grid mesh scheme and a modified Klemp-Durran conditions (Klemp and Wilhelmson, 1978) at the top boundary for TASS model to simulate planetary boundary layer under stable stratification conditions.

During the past year, our group has made great efforts to carry out the above mentioned four tasks simultaneously. The work accomplished in the last year will be described in the next section.

# 2 Work Accomplished During the Period 4/97-3/98

## 2.1 Task 1: Two-Dimensional Simulation of Vortex Decay

In our proposal, we proposed to continue validation of two-dimensional simulation of wake vortex decay, which include investigation of sensitivity of vortex motion to atmospheric environments and vortex model. We studied sensitivity of vortex motion to domain size using TASS-LES model (Proctor, 1987, 1998). Three two-dimensional simulations have been performed. In these simulations, we used the new vortex model proposed by Proctor (1998) and chosen grid size ($\triangle x$, $\triangle z$)=(0.5, 0.5 ). The seperation distance $b_0$ was set to 16m and core radius $r_c$=1m. The domain size were ($L_x$, $L_z$)=($5b_0$, $15b_0$), ($15b_0$, $15b_0$)and ($25b_0$, $25b_0$), respectively.

The results indicate that when domain size is ($5b_0$, $15b_0$), vortex pair deviates significantly from the ideal line, which means horizontal periodic vortices of $5b_0$ distance reduce the descent speed significantly. The descent speed in the case of domain size ($25b_0$, $25b_0$) is the same as that of the domain size ($15b_0$, $15b_0$), which shows small deviation from the ideal line, especially in later dimensionless time.

## 2.2 Task 2: Three-Dimensional Simulation of Wake Vortex Decay

In an effort to investigate the atmospheric turbulence effects on aircraft wake vortices and the length scale for vortex decay and transport, we first studied the effects of ambient turbulence on the Crow instability, the vortex lifetime and the corresponding length scale using TASS-LES model. Then we studied the ambient turbulence effects on vortex decay and descent distance. Based on our LES results, the new algorithms were developed.

### 2.2.1 Initial turbulence field

It is of crucial importance to obtain an initially homogeneous and isotropic turbu-

lence field to simulate the ambient turbulence effects on wake vortex decay. Toward this purpose, a method of artificial external forcing at low wavenumbers of three-dimensional FFT was developed. The forcing was applied at every time step. Due to viscous dissipation, the simulation can reach a statistically steady state in the sense that the mean turbulence kinetic energy (TKE) fluctuates in time around a constant value. Figure 1 shows that the domain averaged TKE and the resolved velocity variances from one of our simulations in which the domain size $(L_x \times L_y \times L_z) = (20b_0 \times 5b_0 \times 5b_0)$ with grid points of $324 \times 112 \times 112$. We can see from Fig. 1 that the turbulence reach a steady state around $1000\,s$.

Figure 2 shows the one-dimensional spectra of $u$ and $v$ in the statistically steady state as functions of wavenumber $\kappa_1$, where subscript 1 represents axial direction. Fairly extensive inertial subranges with

$$F_{11}(\kappa_1)\,{\kappa_1}^{5/3}\,\langle\epsilon_r\rangle^{-2/3} = \alpha_1 \approx 0.67 \tag{1}$$

and

$$F_{22}(\kappa_1)\,{\kappa_1}^{5/3}\,\langle\epsilon_r\rangle^{-2/3} = (4/3)\,\alpha_1 \approx 0.89 \tag{2}$$

are present, where $F_{11}(\kappa_1)$ and $F_{22}(\kappa_1)$ are one-dimensional longitudinal and transverse spectra, respectively, and $\epsilon_r$ represents the TKE dissipation rate estimated from the resolved flow field. After the turbulence reached a steady state, the vortex system was then injected into the model.

### 2.2.2 The Crow instability

Several three -dimensional simulations of different turbulence levels were performed to the effects of ambient turbulence on the Crow instability. In these simulations, the grid points are $324\times112\times112$ with grid size $(\Delta x, \Delta y, \Delta z) = (1.0\,m, 0.75\,m, 0.75\,m)$, where $x$, $y$ and $z$ correspond to the axial, lateral and vertical directions of the vortex system , respectively. Periodic boundary conditions are imposed at all domain boundaries. Two values of $b_0$, i.e., $b_0 = 16\,m$ and $b_0 = 8\,m$, are used for fixed domain size.

For the case of $b_0 = 16\,m$ the domain size becomes $(L_x \times L_y \times L_z) = (20b_0 \times 5b_0 \times 5b_0)$. The larger domain size in the axial direction $(20b_0)$ is nearly the minimum necessary to simulate the most-amplified wavelength of about $8.6b_0$ for Crow instability (Crow, 1970, Crow and Bate, 1987). But, smaller domain size of $5b_0$ in lateral and vertical directions is an acceptable separation for a vortex pair, because the strain rate of neighboring pairs, which are assumed to be present out of domain in periodic boundary conditions, is only a few percent of that exerted by one vortex on the other in the vortex pair.

The vortex system is representative of the post roll-up wake velocity field and is initialized with the superposition of two counter-rotating vortices, with the velocity field for each vortex specified according to the Burnham-Hallock model (Burnham and Hallock, 1982) as

$$V(r) = \frac{\Gamma_0}{2\pi} \frac{r}{{r_c}^2 + r^2}, \tag{3}$$

where $V(r)$ is the vortex tangential velocity at radius $r$, $r_c$ is the core radius (i.e., radius of peak tangential velocity), and $\Gamma_0$ is the circulation at $r >> r_c$. In this study $r_c$ is fixed as $2\,m$.

Figure 3 shows top and side views of the vortex pair with increasing nondimensional time for six different nondimesional turbulence intensities $\eta$. Most of the cases except for stronger turbulence in Fig. 3 clearly show that Crow instability has been developed. In agreement with observations, the vortex pair connects together as a result of the instability, forms a train of vortex rings, and then disintegrates into a turbulent state. For a stronger turbulence, the vortices are more irregularly distorted due to advection by a strong ambient turbulence, but a sinusoidal instability still appears to develop. This vortex behavior for stronger turbulence was observed by Tombach (1973). Spalart and Wray's (1996) direct numerical simulation (DNS) study also shows similar patterns, but their results for intense turbulence appear to

be dominated by advection of ambient turbulent flow without the indication of the sinusoidal development of Crow instability.

In the top views of Fig. 3, the maximum unstable wavelength (MUW) appears to decrease with increasing turbulence intensity. A quantitative estimate of the MUW can be obtained from the spectrum analysis of $y-$displacement of the vortex along the axial direction just before vortex linking. The MUW for $\eta = 0.0316$, 0.0789, and 0.1753 ranges from $4b_0$ to $7b_0$, showing higher value for weaker turbulence. For stronger turbulence (i.e., $\eta = 0.3506$ and 0.5844), a significant spectral energy of the displacement can be seen in the smaller wavelength range. The laminar run shows the largest MUW, i.e., about $10b_0$. This trend that the MUW decreases with increasing turbulence intensity agrees surprisingly well with results of Liu (1992) laboratory experiments. It is noticeable that stronger turbulence tends to more strongly intensify smaller unstable wavelengths than larger ones.

### 2.2.3 Vortex lifetime

Following Crow and Bate (1978)'s definition, the vortex lifetime or lifespan is defined as the time at which linking of a vortex pair occurs. According to Crow and Bate (1978) (hereafter, CB), the vortex lifespan in weak turbulence is given by

$$\eta = a''\tau^{1/4}e^{-0.83\tau} = 0.87\tau^{1/4}e^{-0.83\tau}. \tag{4}$$

We re-evaluate $a''(\kappa_m)$ based on our LES results and find that the approximate coefficient is about 4.90 instead of 3.12 from a parabolic fit to the amplification rate curve. With this refined value, the vortex lifespan for weak turbulence is

$$\eta = 0.98\tau^{1/4}e^{-0.83\tau}. \tag{5}$$

Fig. 4 shows that the new expression gives a larger lifespan for given $\eta$ than the original one, but the difference between $Eq.(4)$ and $Eq.(5)$ is rather small. Despite large difference in $R_e$ between LES and water tank experiment, the LES results agree

surprisingly well with Sarpkaya and Daly's (1987) experiment. The results from our LES show vortex lifespan is primarily controlled by dimensionless turbulence intensity $\eta$ and decreases with increasing $\eta$, while the integral scale of turbulence is of minor importance to vortex lifespan. The lifespan is estimated to be about 40 % larger than that in the theoretical prediction by CB in which the ambient atmospheric turbulence is regarded as independent of the vortices. These larger lifespans is caused by slower growth in the middle of the vortex lifespan, probably due to the nonlinear interaction between the vortices and the ambient atmospheric turbulence.

### 2.2.4 Ambient turbulence effects on vortex decay

We have performed three-dimensional simulations of ambient atmospheric turbulence's impacts on the circulation decay and descent distance. In these simulations, domain size: $(L_x, L_y, L_z) = (2.5b_0, 5b_0, 5b_0)$ and $b_0 = 32\,m$. Grid points are $(80\triangle x, 160\triangle y, 160\triangle z)$ with $\triangle x{=}\triangle y{=}\triangle z{=}1m$. The core size of vortex radius, $r_c = 4\,m$. The flow rotation effect is incorporated in the Smagorinsky model (Proctor, 1998). We first investigated the impacts of atmospheric turbulence on the vortex circulation. Then we developed an algorithm to predict the decay of wake vortices in terms of LES results.

Figure 5 shows the vortex decay and tangential velocity with and without rotation effect under different turbulence levels. The impacts of ambient turbulence on vortex pair and single vortex are also shown in the Figure 5. The results show that decay of the normalized circulation increases with increasing ambient turbulence strength but decreases when radial radius is far from vortex center. Compared with results from single vortex, the circulation decay of a pair of vortex is much more enhanced due to enhanced stretching of turbulent eddies exerted by the vortex pair. It appears that it is necessary to incorperate flow rotation effect at the subgrid model, otherwise, the circulation decay around half separation distance is underestimated, especially in earlier time due to unrealistic core expansion.

### 2.2.5 Vortex decay models (algorithms)

Two types of new vortex decay models (algorithms) are proposed based on our LES results and the algorithms proposed by Greene (1986) and Sarpkaya (1998). They are, respectively, Exponential Decay Model:

$$\frac{\Gamma}{\Gamma_0} = e^{-c_1 \frac{\eta}{R^2} T}, \tag{6}$$

and Gaussian Decay Model:

$$\frac{\Gamma}{\Gamma_0} = e^{(-c_2 \frac{\eta^2}{R^2} T^2)}, \tag{7}$$

Analysis of the average circulation from $r = 2.5r_c$ to $r = 0.5b_0$ (Figure 6) shows that for weak and moderate ambient turbulence levels, the vortex decay follows the Gaussian decay type, while for strong ambient turbulence level, it follows exponential decay type. The new algorithm will be validated using Memphis data in this year.

## 2.3 Task 3: ABL Studies

### 2.3.1 Grid-Nesting Scheme

Modification of the nested version of TASS code has been performed. A nesting scheme used by Chen (1991) was implemented in the TASS-LES model. A fine mesh with high resolution overlaps a coarse mesh with low resolution. The fine grid boundary points are interpolated from the coarse mesh in time as well as in space. To avoid wave reflection on the lateral boundaries, the nested radiation boundary condition (Chen, 1991) was used,

$$\frac{\partial \phi}{\partial t} = \frac{\partial \Phi}{\partial t} - C_{\phi-\Phi} \frac{\partial(\phi - \Phi)}{\partial x}, \tag{8}$$

where $\phi$ is a fine mesh variable, $\Phi$ is the same coarse mesh variable interpolated to the fine mesh position, and $C_{\phi-\Phi}$ is the gravity wave phase speed of $\phi$-$\Phi$.

There is an option to use one-way or two-way nesting. With the one-way nesting, the coarse is run indepdently of the fine mesh and the boundary conditions for the fine mesh are interpolated in time as well as space. Under the two-way nesting, the variables in the fine mesh are averaged spatially to update the coarse grid variables in the overlapping region.

Figures 7a and 7b show schematic diagrams of the spatial and temporal arrangements, respectively, of two nested grids. To demonstrate our nesting scheme, a number of tests have been made. One of them is a rising symmetric temperature impulse and its interaction with a strong inversion. The coarse mesh domain is $50\times50\times75$ with 40m resolution in both horizontal directions and 20m resolution in the vertical direction. The fine mesh domain size is $40\times40\times132$. The resolution in the nesting mesh is twice smaller than the coarse mesh. The potential temperature of the environmental is set to be constant below about 900m and constant above with a sharp 16 degree inversion between. The temperature impuse had an initial radius of 200m with a peak amplitude of $2^0$C. One way nesting is employed in this simulation.

Figure 8 shows potential temperature contours in a central vertical plane of the simulation at 12 min and 16 min. A finer detail of the wave structure is observable in the nested fine-mesh grid. At 16 min, most of the potential temperature disturbance has passed out of the fine mesh without reflecting off the boundary, indicating the success of the nested radiation boundary condition. The contours of the y-component of vorticity on the same planes as Figure 8 is given in Figure 9. We observe this ring moves across the boundary smoothly. The fine mesh gives a better resolution of residual vorticity at the center of the domain as well as higher gradients in the baroclinic ring. These are precisely the types of details which are important for wake vortex numerical experiments.

We also have run three 'baseline' convective boundary layer (CBL) simulations which were compared with the nested-grid simulation results. The domain of the

three 'baseline' simulation are 5×5×2km, 2.5×2.5×2km and 2.5×2.5×2km with the resolution of 50×50×50m, 50×50×50m and 25×25×25m, respectively. The results from the nested-grid simulations with nesting mesh agree well with those from baseline simulations.

### 2.3.2 The baroclinic effects during PBL transition

During the evening transition, the atmospheric boundary layer evolves from the convective to the stable state, bridging the two extremes. The boundary layer transition period is of particular interest because the turbulence decays while the mean wind near the surface decelerates. Nieuwstadt and Brost (1986) and Sorbjan (1997) described the decay of turbulence of convective boundary layer. We simulated the barolinic effects on the turbulence decay during the evening transition.

The baroclinicity in atmosphere, M=$(M_1{}^2 + M_2{}^2)^{1/2}$, can be expresssed in terms of nondimensional geostrophic windspeed shear:

$$M_1 = \frac{z_i}{u_*}\frac{\partial U_g}{\partial z}, \tag{9}$$

$$M_2 = \frac{z_i}{u_*}\frac{\partial V_g}{\partial z}, \tag{10}$$

Two simulations have been performed. One is with resolution of 125m in horizontal directions and 50m in vertical direction. The surface heat flux is 0.12kms$^{-1}$. The other has resolution of 80m in horizontal directions and 30m in vertical direction with surface heat flux of 0.04kms$^{-1}$. Geostrophic wind is 5m/s. Figure 10 shows the turbulence decay under different baroclinic conditions. The results indicate that the decay of convective turbulence is slower than that under barotropic conditions, due to stronger wind shear under baroclinic conditions. Surface heat flux is another important factor which influence the decay of convective turbulence.

## 2.4 Task 4: Klemp-Durran Boundary Condition

In order to eliminate the reflection of gravity waves from the upper boundary, the modified Klemp-Durran method was incorporated into the TASS code. The modified Klemp-Durran scheme can be expressed as:

$$p_k = \rho_0 \frac{N w_k}{(k^2{}_x + k^2{}_y)^{1/2}}, \tag{11}$$

Here p and w are perturbation pressure and vertical velocity, respectively. $\rho$ is air density and $N$ is Brunt-Vaisala frequency. The subscript $k$ notation represents a two-dimensional horizontal Fourier transform at the top boundary. $k_x$ and $k_y$ are the wavenumbers in the x- and y-directions, respectively.

The difficulty for this work is that an implicit scheme must be applied to both the vertical velocity and pressure at the small time step. In other words, the two equations for vertical velocity and pressure have to be solved simultaneously, which result in solving a triangle matrix. A number of testing simulations have been performed and the results are quite good. Figure 11 shows that the implicit scheme of solving the pressure and vertical velocity simultaneously, which is successful for the Klemp-Durran type of upper boundary condition in the bubble experiments.

# 3 Publications in FY 97

Han,J., Y.-L. Lin, D. G. Schowalter, S. P. Arya and P. H. Proctor, 1998: Large eddy simulation of aircraft wake vortices in homogeneous atmospheric turbulence. Part 1. The Crow instability. Submitted to J. of Aircraft.

DeCroix, D. S., D. G. Schowalter, Y.-L. Lin, S. P. Arya and P. H. Proctor, 1997: A three-dimensional nested-grid large eddy simulation of the convective planetary boundary layer. *12th Symposium on boundary layers and turbulence*, American Meteorology Society, Vancouver, BC, Canada.

Han,J., Y.-L. Lin, D. G. Schowalter, S. P. Arya and P. H. Proctor, 1997: Large eddy simulation of aircraft wake vortices: Atmospheric turbulence effects. *12th Symposium on boundary layers and turbulence*, American Meteorology Society, Vancouver, BC, Canada.

# 4 References


[1] Burnham, D. C. and Hallock, J. N., "Chicago Monostatic Acoustic Vortex Sensing System, Vol. 4: Wake Vortex Decay," Springfield, VA, NTIS, 1982.

[2] Chen, C., A nested grid, nohydrostatic, elastic modeling using a terrain-following corrdinate transformation: The radiative-nesting boundary conditions. *Mon. Wea. Rev.*, 119, pp 2852-2869, 1991.

[3] Crow, S.C., "Stability Theory for a Pair of Trailing Vortices," *AIAA Journal*, Vol. 8, 1970, pp. 2172-2179.

[4] Crow, S. C. and Bate, E. R., "Lifespan of Trailing Vortices on a Turbulent Atmosphere,"

[5] Greene, G. C., "An Approximate Model of Vortex Decay in the Atm osphere," *Journal of Aircraft*, Vol. 23, 1986, pp. 566-573.

[6] Klemp, J. B. and Wilhelmson, R. B., The simulation of three-dimensional convective storm dynamics, *J. Atmos. Sci.*, Vol. 35, pp 1070-1096, 1978.

[7] Liu, H. -T., "Effects of Ambient Turbulence on the Decay of a Tr ailing Vortex Wake," *Journal of Aircraft*, Vol. 29, 1992, pp. 255-263.

[8] Nieuwstadt, F. T. M. and Brost, R. A., The decay of convective turbulence, *J. Atmos. Sci.*, Vol. 43, pp 532-546, 1986.

[9] Proctor, F. H., The Terminal Area Simulation System Volume I: Theoretical Formulation. NASA Contractor Report 4046 DOT/FAA/PM-86/50, 1987.

[10] Proctor, F. H., NASA-Langley wake vortex modeling effort in support of an operational aircraft spacing system. *AIAA Journal*, 1998.

[11] Sarpkaya, T. and Daly, J. J., "Effect of Ambient Turbulence on T railing Vortices," *Journal of Aircraft*, Vol. 24, 1987, pp. 399-404.

[12] Spalart, P. R. and Wray, A. A., "Initiation of the Crow Instabil ity by Atmospheric Turbulence," *78th AGARD-FDP Symposium on The Characterization and Modific ation of Wakes from Lifting Vehicles in Fluids*, Trondheim, Norway, 20-23 May 1996.

[13] Sarpkaya, T., "Decay of Wake Vortices of Large Aircraft," *36th Aerospace Sciences Meeting & Exhibit*, Reno, NV, AIAA Paper No. 98-0592, January 1998.

[14] Sorbjan, Z., Decay of convective turbulence revisited. *Boundary-Layer Meteorol.*, Vol. 82, 501-515, 1997.

[15] Tombach, I., "Observations of Atmospheric Effects on Vortex Wake Behavior," *Journal of Aircraft*, Vol. 10, 1973, pp. 641-647.

# 5 List of Figures

Figure 1. Time evolution of turbulent kinetic energy and velocity variances before vortex injection.

Figure 2. One-dimensional energy spectrum in a steady state turbulence before vortex injection.

Figure 3. Top ($x$, $y$) and side (($x$, $z$) views of wake vortices at seven non-dimensional times for the case of $b_0$=16m: (a) the laminar case; (b) $\eta$=0.0316; (c) $\eta$=0.0789; (d) $\eta$=0.1753; (e) $\eta$=0.3506; (f) $\eta$=0.5844.

Figure 4. Dimensionless vortex lifespans from numerical simulations, laboratory experiments, and flight tests.

Figure 5. Radial distribution of circulation and tangential velocity with time for $\eta$=0.1509; (a) and (b): Vortex pair with flow rotation modification in the original Smagorinsky model; (c) and (d): vortex pair without flow rotation modification; (e) and (f): single vortex with flow rotation modification.

Figure 6. Decay of averaged circulation from r=2.5$r_c$ to r=0.5$b_0$ and corresponding analysis function for varying ambient turbulence level.

Figure 7. Schematic diagram of (a) spatial and (b) temporal arrangement of two nested grids. x denotes locations for velocity values and o denotes scalar locations on the Arakawa C staggered mesh. $dt_1$ is the times step for the coarse mesh and $dt_2$ is for the fine mesh.

Figure 8. Contours of potential temperature for coarse and fine mesh simulations at 12 and 16min of simulation time in the central x-z plane, where z is the vertical axis. (a) and (c) are for coarse mesh simulations while (b) and (d) are for fine mesh simulations. (a) and (b) are at 12min of simulation time while (c) and (d) are at 16min.

Figure 9. Same as Figure 8 but contours are for vorticity in the y-direction.

Figure 10. Averaged turbulence kinetic energy evolution for barolinic intensity.

Figure 11. Contours of vertical velocity for the warm bubble experiment in x-Z plane.

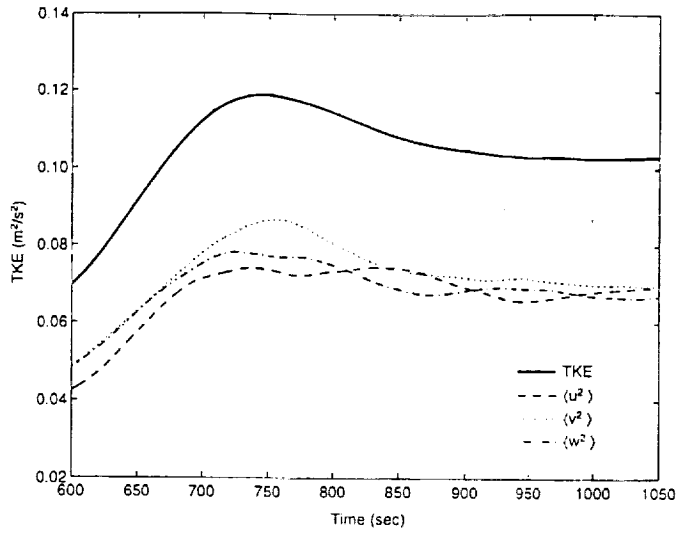


Figure 1: Time evolution of turbulent kinetic energy and velocity variances before vortex injection.

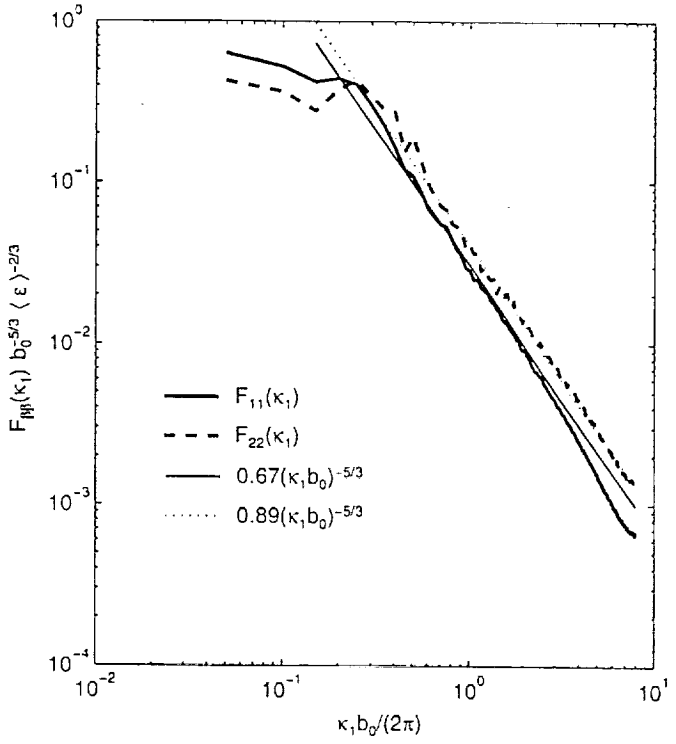


Figure 2: One-dimensional energy spectrum in a steady state turbulence before vortex injection.

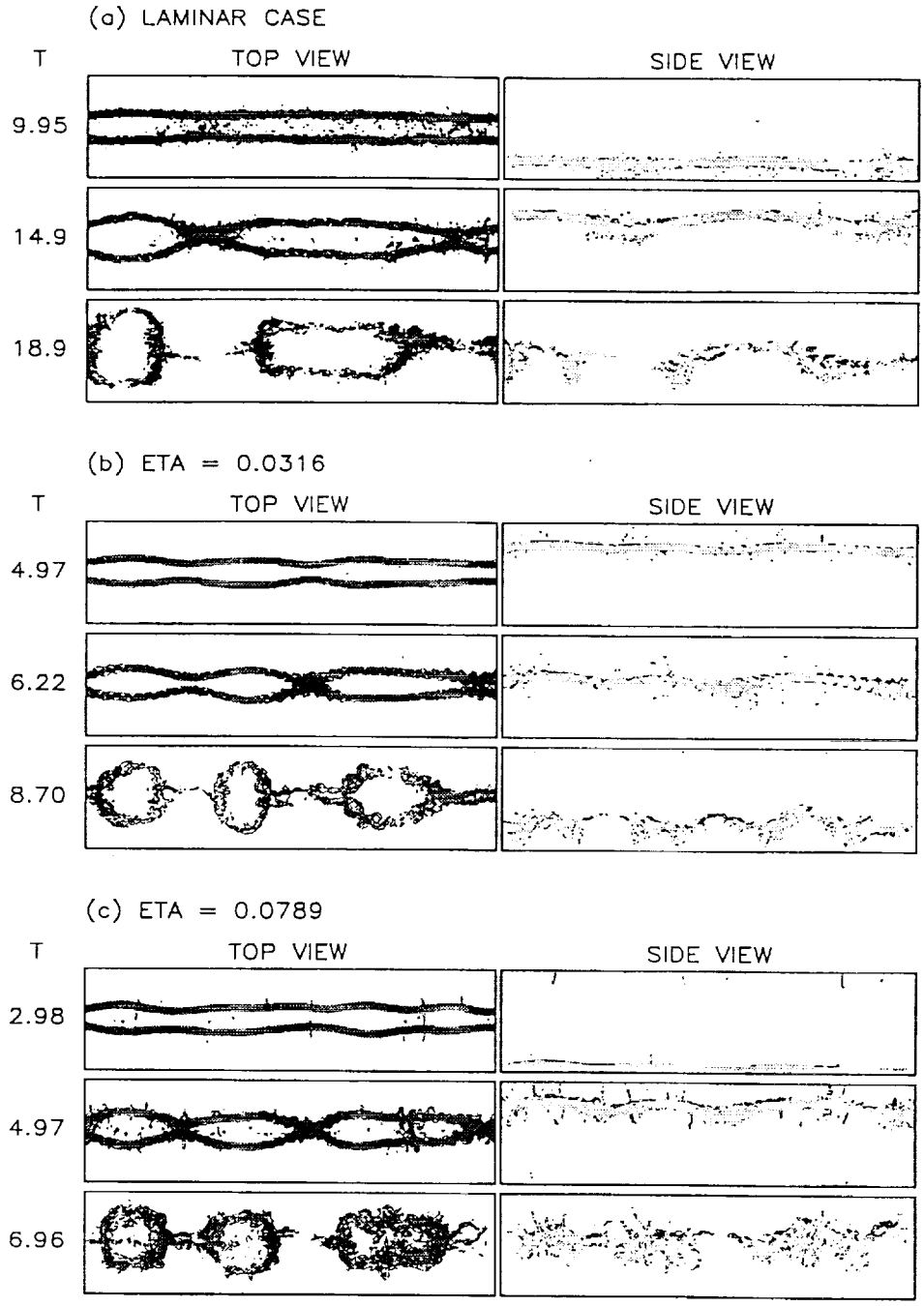


Figure 3: Top $(x, y)$ and side $(x, z)$ views of wake vortices at seven nondimensional times for the case of $b_0 = 16\,m$: (a) the laminar case; (b) $\eta = 0.0316$: (c) $\eta = 0.0789$: (d) $\eta = 0.1753$; (e) $\eta = 0.3506$; (f) $\eta = 0.5844$.

(d) ETA = 0.1753

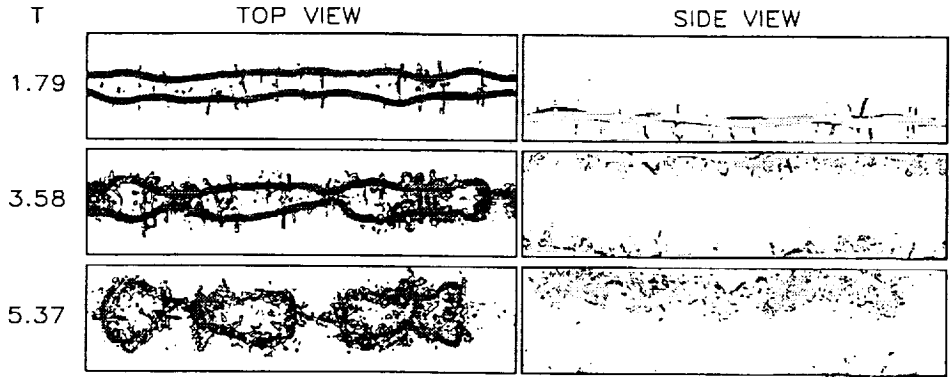


(e) ETA = 0.3506

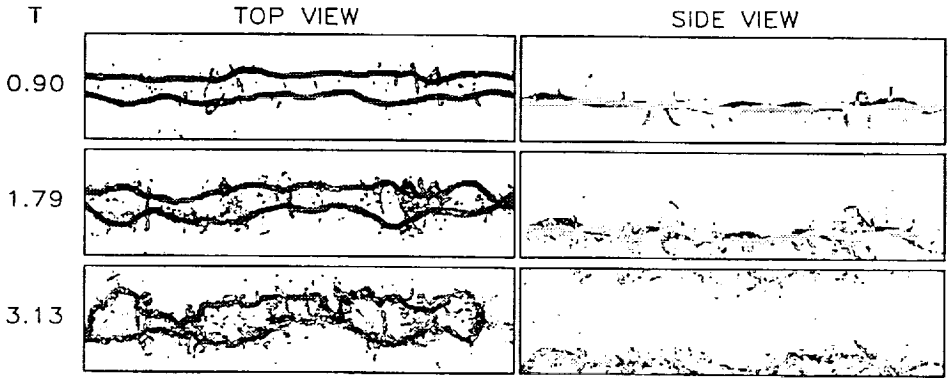


(f) ETA = 0.5844

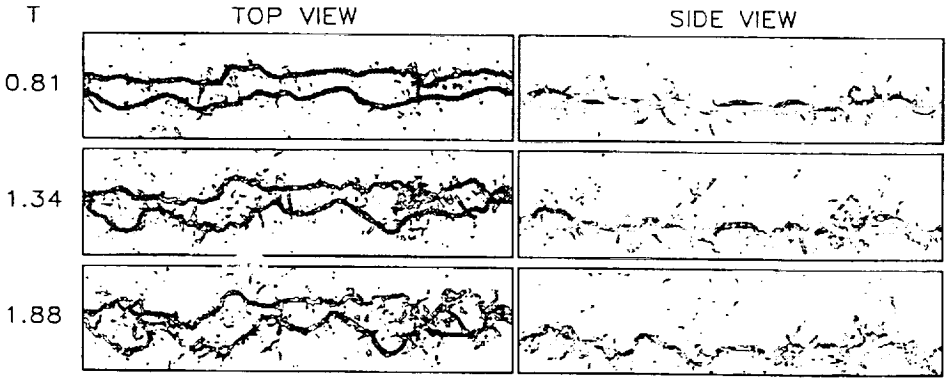

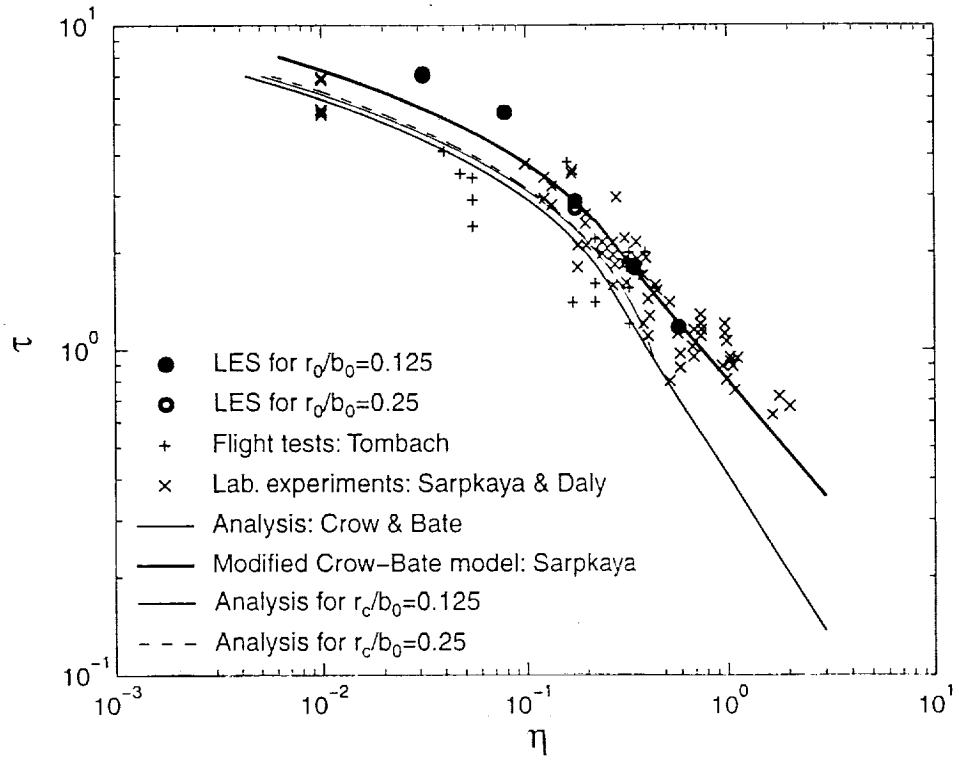


Figure 4 Dimensionless vortex lifespans from numerical simulations, laboratory experiments, and flight tes[illegible].

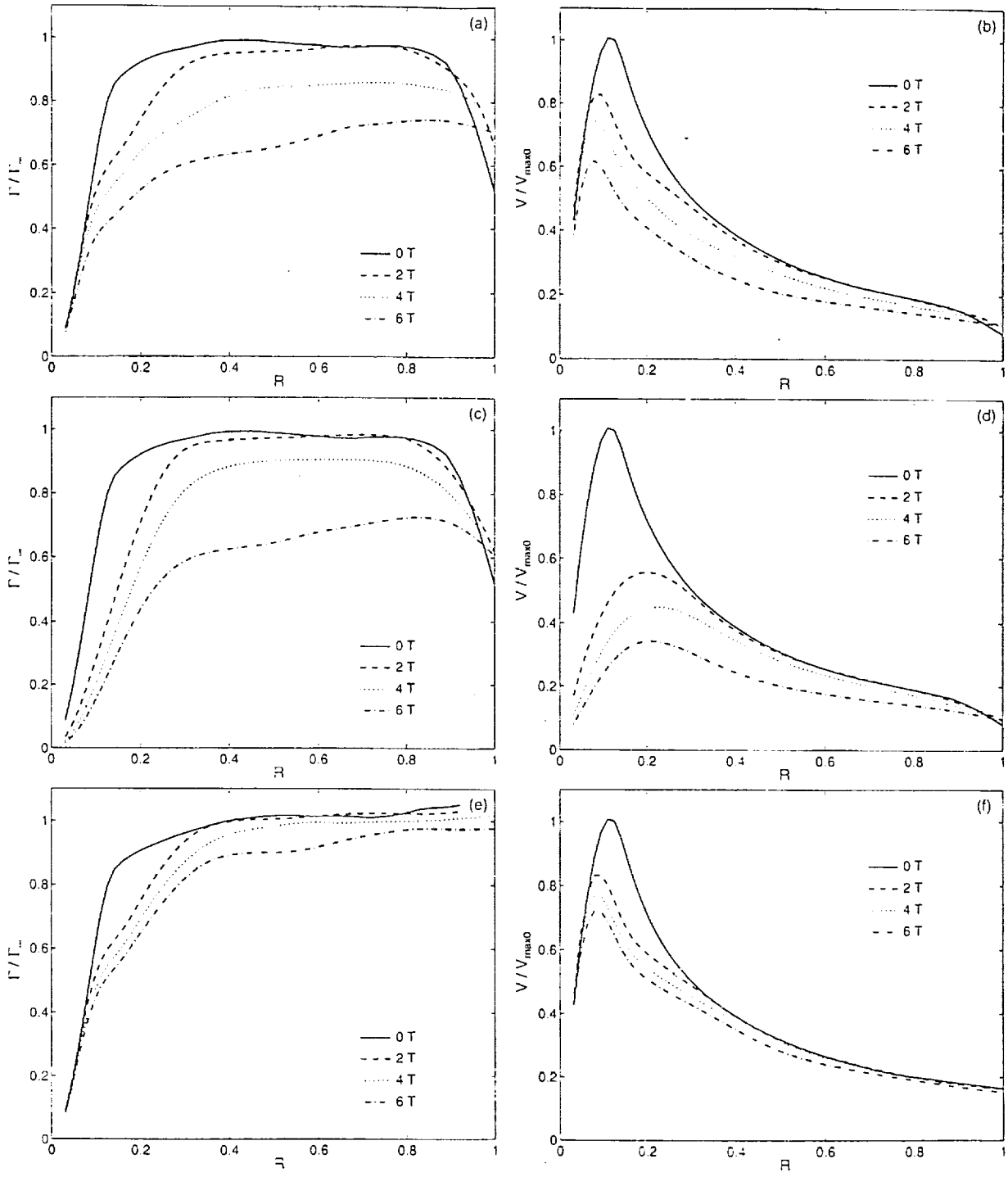


Figure 5. Radial distribution of circulation and tangential velocity with time for $\eta$=0.1509; (a) and (b): Vortex pair with flow rotation modification in the original Smagorinsky model; (c) and (d): vortex pair without flow rotation modification; (e) and (f): single vortex with flow rotation modification.

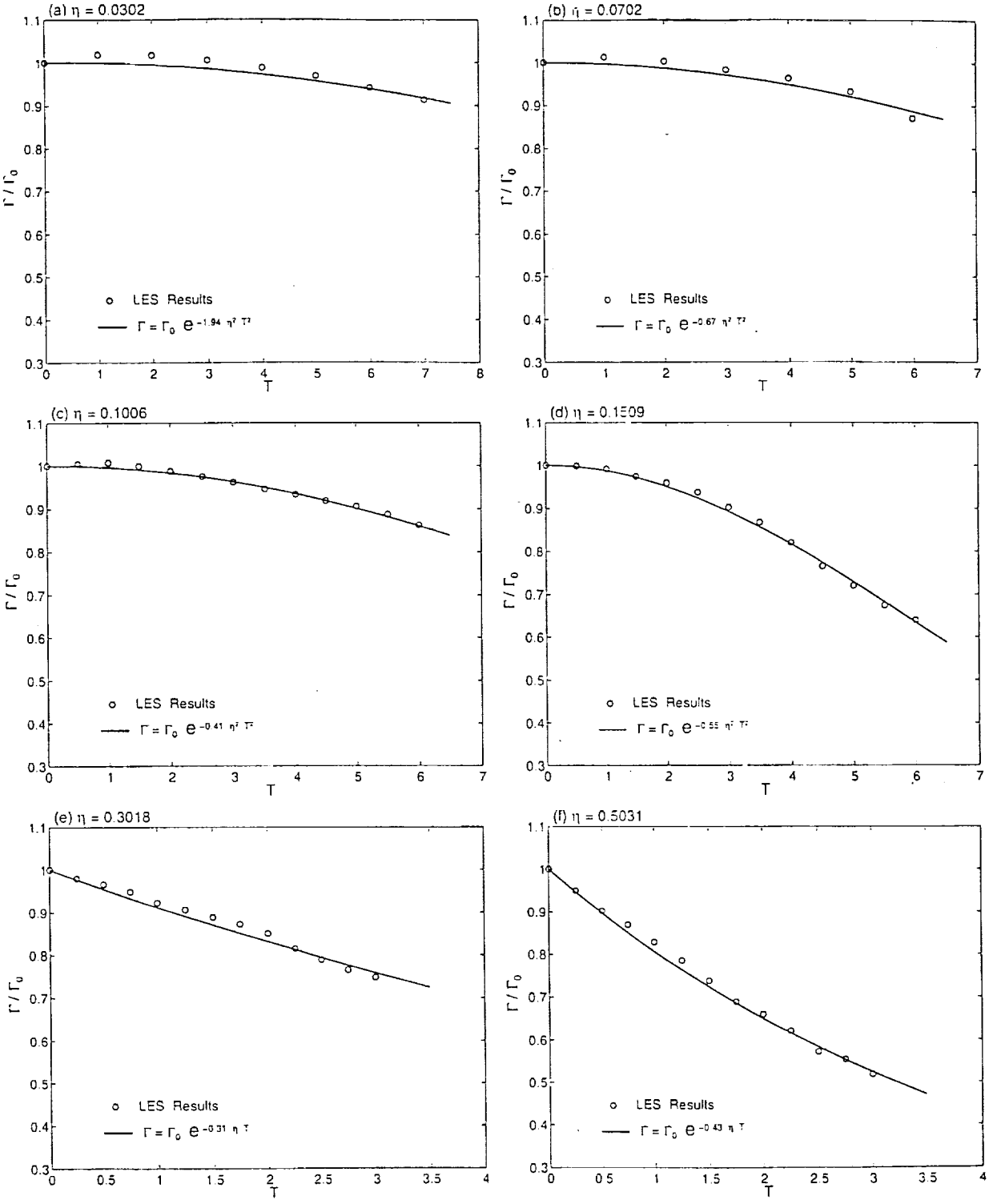


Figure 6 Decay of averaged circulation from $r = 2.5\,r_c$ to $r = 0.5\,b_0$ and corresponding analysis function for varying ambient turbulence level.

(a)

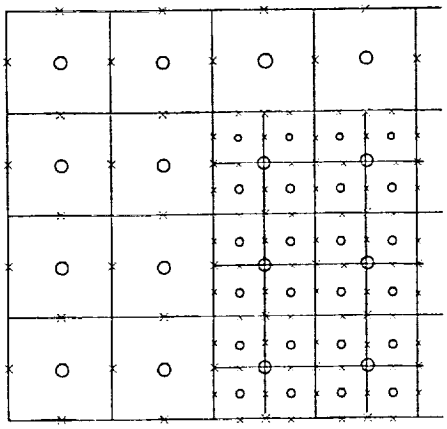

(b)

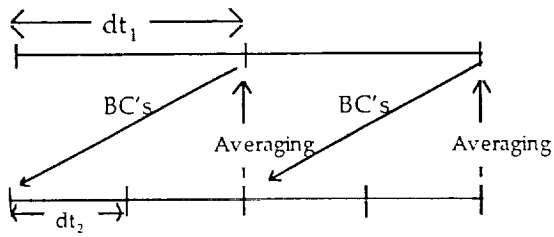


**Figure** 7 Schematic diagram of (a) spatial and (b) temporal arrangement of two nested grids. × denotes locations for velocity values and O denotes scalar locations on the Arakawa C staggered mesh. The nesting ratio is two for both directions shown. $dt_1$ is the time step for the coarse mesh and $dt_2$ for the fine mesh. Boundary conditions pass from the coarse mesh to the fine mesh and, if two-way nesting is specified, averaging information for the variables is passed back to the coarse mesh at the indicated times.

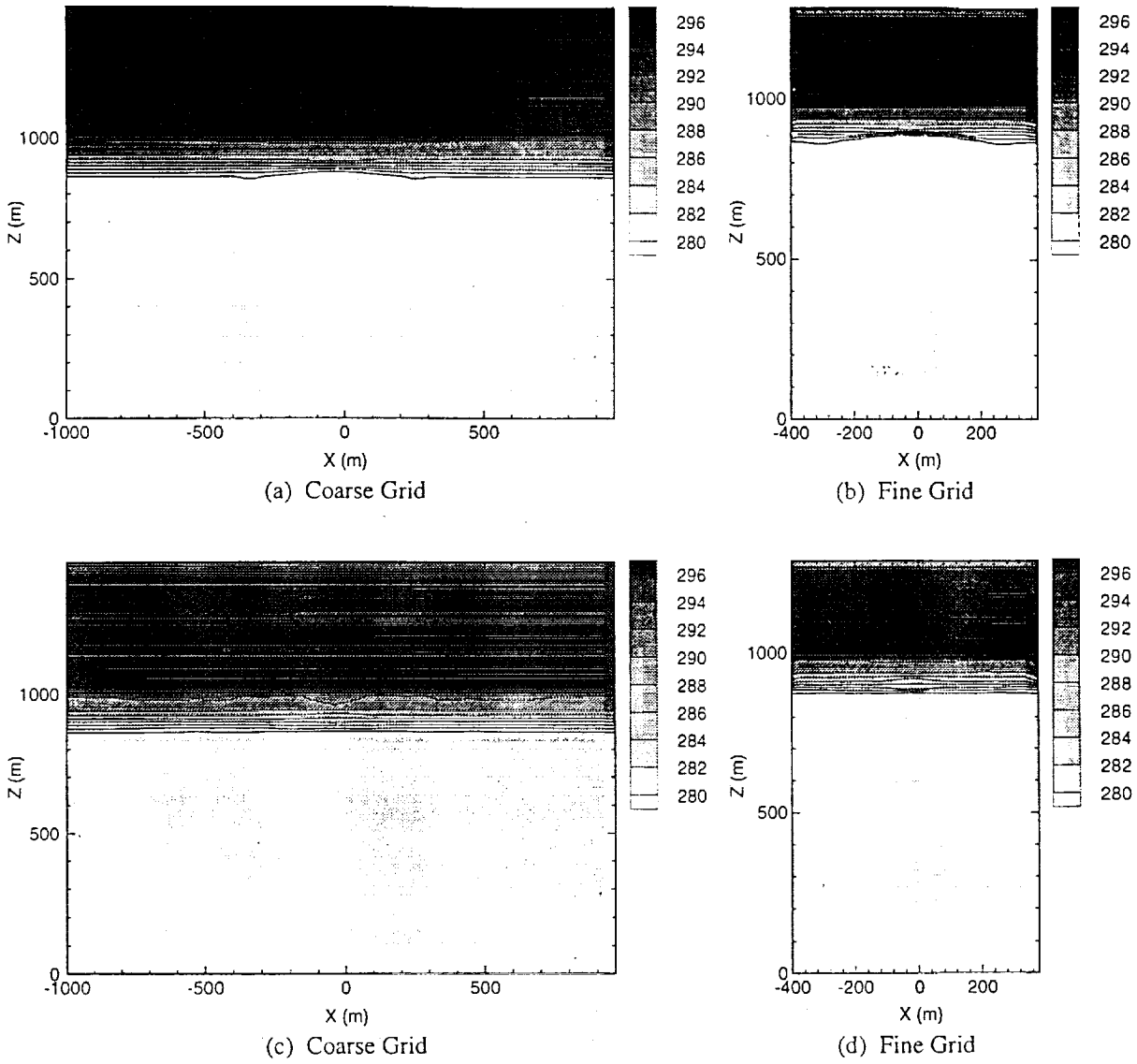


**Figure 8** Contours of potential temperature for coarse and fine mesh simulations at 12.0 and 16.0 minutes of simulation time in the central $x$-$z$ plane, where $z$ is the vertical axis, (a) and (c) are for coarse mesh simulations while (b) and (d) are for fine mesh simulations. (a) and (b) are at 12.0 minutes of simulation time while (c) and (d) are at 16.0 minutes.

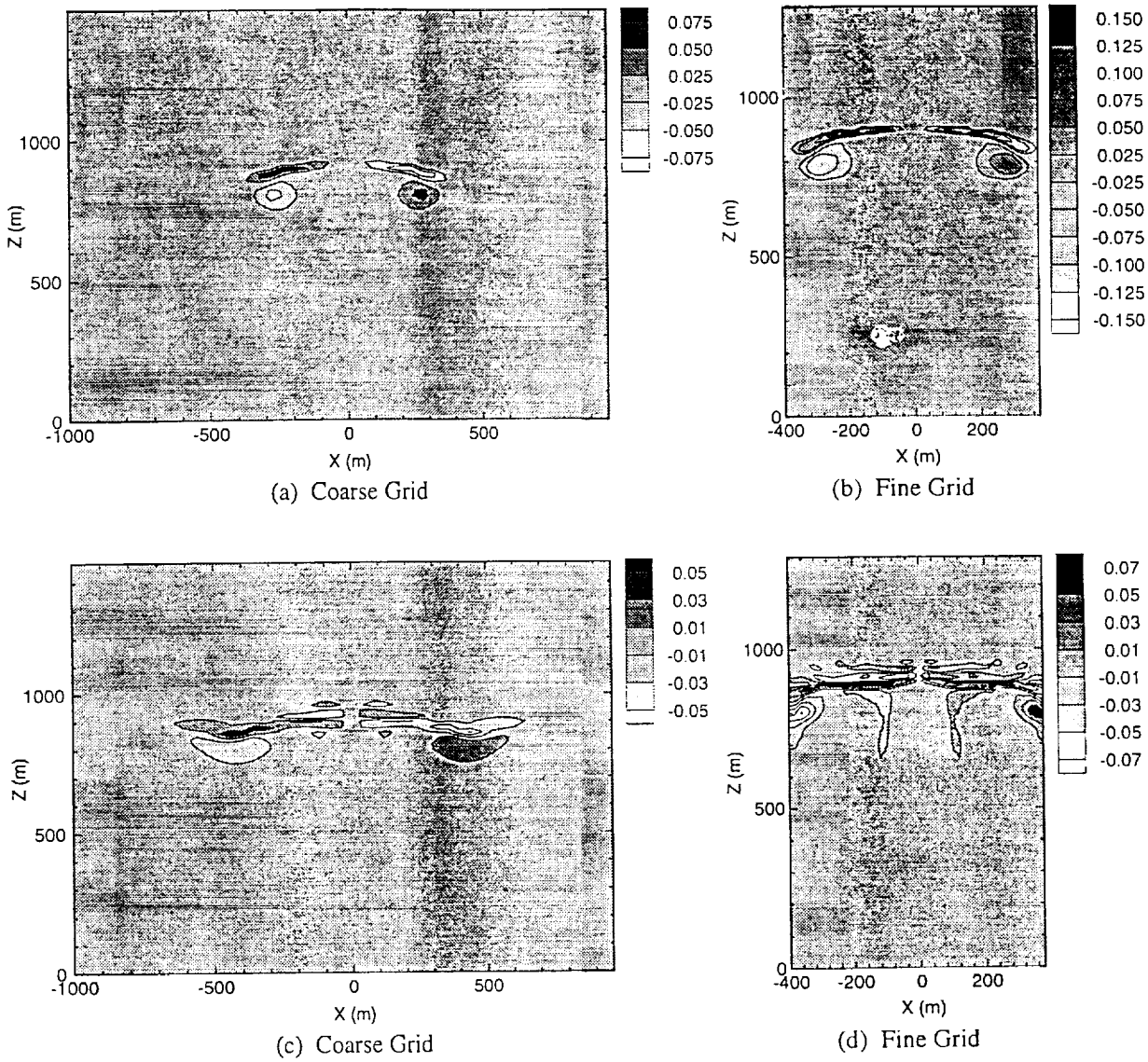


Figure 9 Same as Figure 8 but contours are for vorticity in the y-direction.

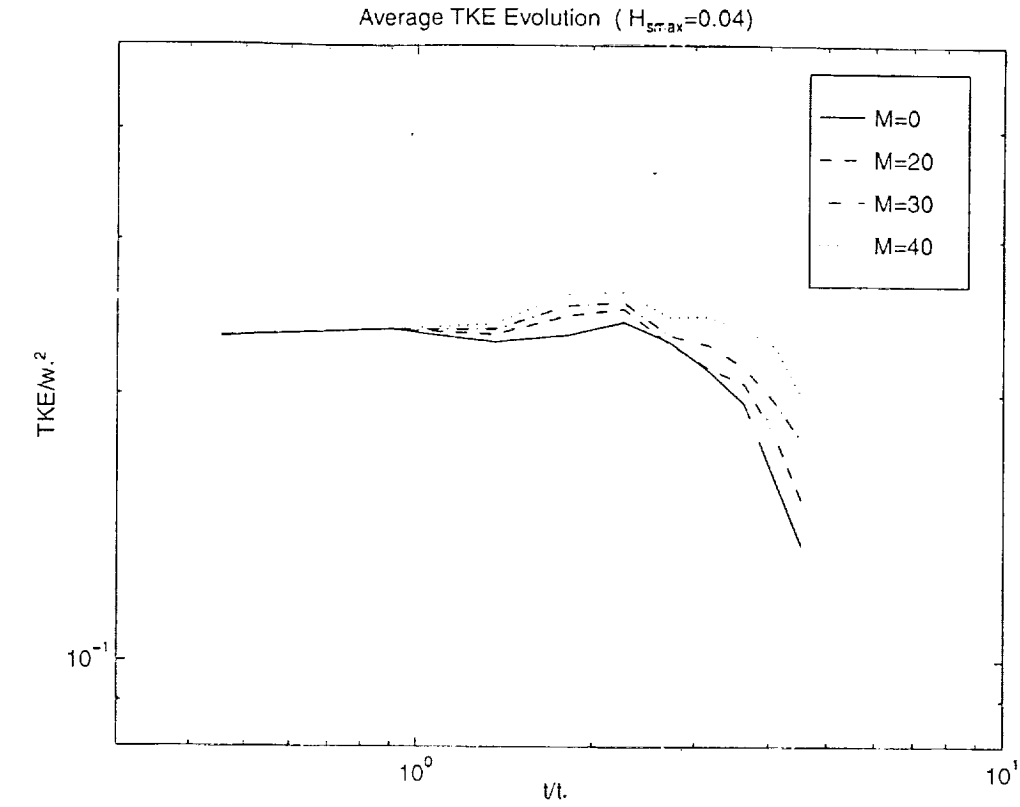


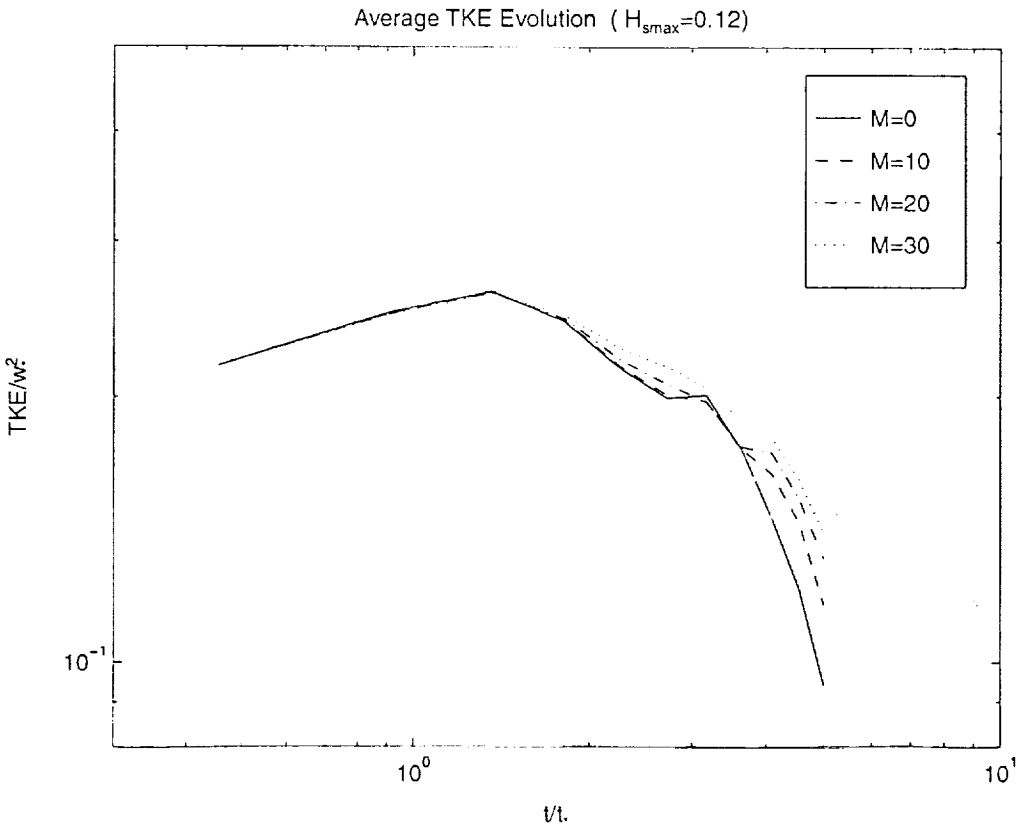


Figure 10. Averaged turbulence kinetic energy evolution for barolinic intensity.

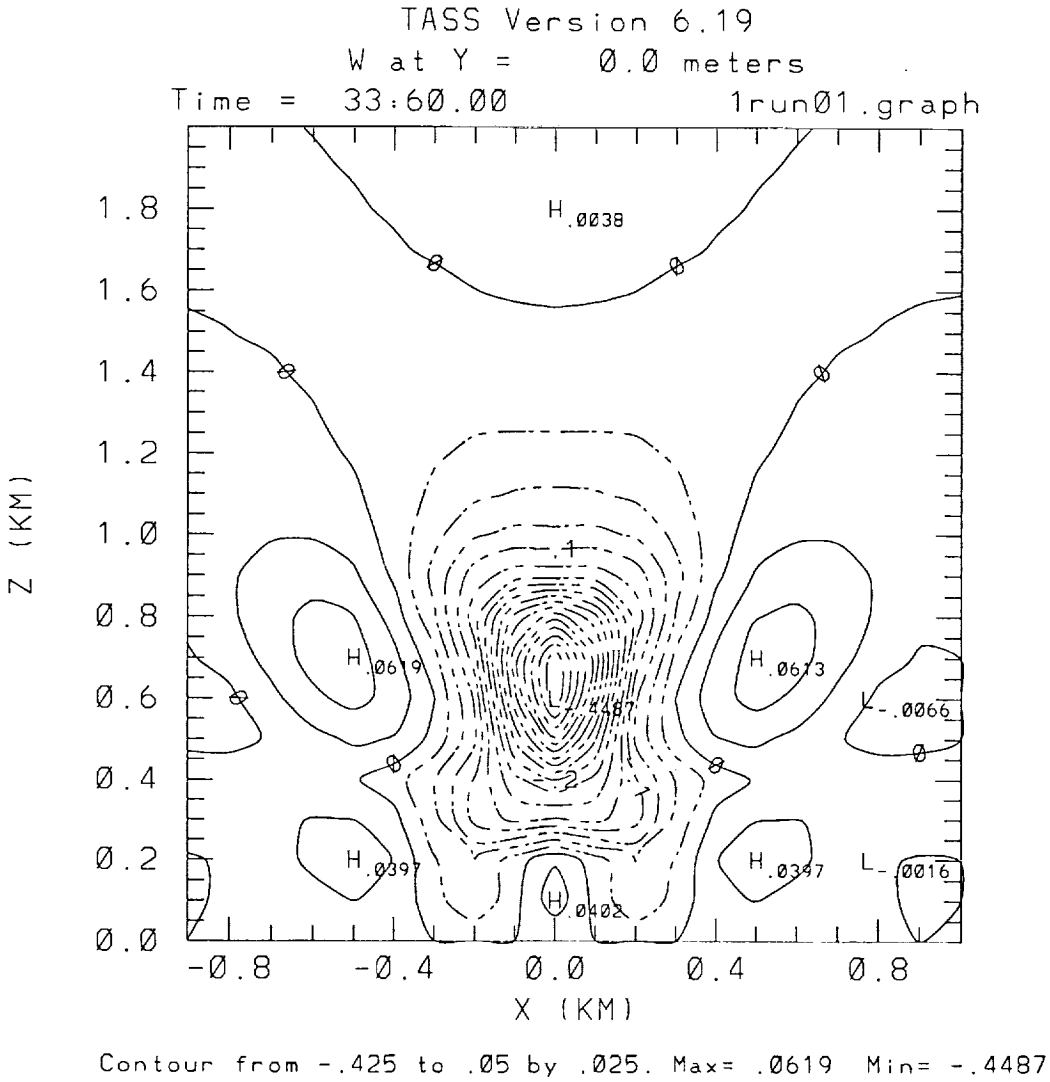


Figure 11. Contours of vertical velocity for the warm bubble experiment in x-Z plane.